



# **1 Influence of Major Sudden Stratospheric Warming With Elevated 2 Stratopause on the Hydroxyl in the Polar Middle Atmosphere**

3  
4 **Jin Hu<sup>1</sup>, Sheng-Yang Gu<sup>1\*</sup>, Yusong Qin<sup>1\*</sup>, Yuxuan, Liu<sup>1</sup>, and Yafei Wei<sup>1</sup>**

5 <sup>1</sup>School of Earth and Space Science and Technology, Wuhan University, Wuhan, China

6 \*Corresponding author: Sheng-Yang Gu ([gushengyang@whu.edu.cn](mailto:gushengyang@whu.edu.cn)) & Yusong Qin  
7 ([qinyusong@whu.edu.cn](mailto:qinyusong@whu.edu.cn)), School of Earth and Space Science and Technology, Wuhan  
8 University, Wuhan, China.  
9

10 **Abstract:** Based on the specified dynamics simulation of Whole Atmosphere  
11 Community Climate Model with ionosphere/thermosphere extension (SD-WACCM-X),  
12 the composite response of polar Hydroxyl (OH) layer in the mesosphere and lower  
13 thermosphere (MLT) to the Arctic major sudden stratospheric warming (SSW) events  
14 with elevated stratopause (ES) during 2004–2023 is investigated. A total of ten ES-SSW  
15 events are systematically analyzed. Before the onset of ES-SSW events, the OH  
16 concentration climatologically peaks at  $7.4 \times 10^{-9}$  mol/mol near  $\sim 82.4$  km. During the  
17 stratospheric warming phase, relative to the climatology, the peak height of OH layer  
18 undergoes a distinct upward displacement reaching  $\sim 85.9$  km accompanied by a  
19 reduction in the OH concentration to  $2.9 \times 10^{-9}$  mol/mol. This shift is closely linked to  
20 an  $\sim 11\%$  and  $\sim 90.8\%$  reduction in mesospheric temperature and atomic oxygen,  
21 respectively, due to enhanced upward residual circulation. During the elevated  
22 stratopause phase, the peak height of OH layer experiences a pronounced downward  
23 shift to  $\sim 80.6$  km with a maximum in OH concentration to  $6.8 \times 10^{-9}$  mol/mol. This  
24 phase is characterized by  $\sim 3.7\%$  and  $\sim 137.3\%$  enhancements in mesospheric  
25 temperature and atomic oxygen concentrations, respectively, which is driven by  
26 intensified downward residual circulation. Further analysis suggests that OH  
27 concentration variations are positively correlated to mesospheric temperature  
28 anomalies and atomic oxygen redistribution induced by vertical transport, which is  
29 attributed to the significant influence of ES-SSW on gravity wave drag (GWs) in the  
30 mesosphere.  
31  
32



## 33 **Key Points**

- 34 1. The peak height of Arctic OH layer rises during the stratospheric warming phase  
35 and descends during the elevated stratopause phase.
- 36 2. The change in OH concentration during ES-SSW shows a significant positive  
37 correlation with the change in mesospheric atomic oxygen concentration and  
38 temperature.
- 39 3. The vertical circulation anomalies due to the variations in gravity wave drag during  
40 ES-SSW alter the mesospheric atomic oxygen concentration and temperature.

## 42 **1. Introduction**

43 The middle atmosphere, spanning from ~20 to 100 km in altitude, plays a vital  
44 role in coupling different atmospheric layers and modulating space weather phenomena.  
45 Hydroxyl (OH) is a key component in the MLT region, exerting an essential function  
46 in atmospheric chemistry and serving as an important indicator for assessing the  
47 atmospheric thermal budget. In the mesopause region, OH is primarily produced  
48 through the reaction between ozone and atomic hydrogen, forming excited OH\* near  
49 87 km. This excited state is deactivated either via photon emission in the Meinel bands  
50 (observed as nightglow) or by collisional quenching. The latter process prevails at lower  
51 altitudes, where higher atmospheric density facilitates the formation of a ground-state  
52 OH layer near 82 km (Damiani et al., 2010).

53 Despite the relatively well-understood chemical formation of OH, comprehensive  
54 observational characterization of its variability remains limited. Nevertheless,  
55 measurements from ground-based instruments and satellites, such as Thermosphere  
56 Ionosphere Mesosphere Energetics and Dynamics (TIMED)/Sounding of the  
57 Atmosphere using Broadband Emission Radiometry (SABER) and Aura Microwave  
58 Limb Sounder (MLS), have provided a valuable opportunity to examine OH variability  
59 (Gao et al., 2011; Damiani et al., 2010; Medvedeva et al., 2019). Shapiro et al. (2012)  
60 identified a positive correlation between mesospheric OH variability and 27-day solar  
61 irradiance cycles, with stronger responses observed during periods of heightened solar  
62 activity. Minschwaner et al. (2011) further demonstrated that ultraviolet actinic flux  
63 serves as the primary driver of OH diurnal variability. Li et al. (2005) observed that OH



64 concentrations peak near local noon, followed by a pronounced decline during  
65 nighttime. Additionally, statistical analyses by Gao et al. (2010, 2011, 2016) on the  
66 temporal and spatial distributions of OH and O<sub>2</sub> nightglow emissions highlighted  
67 significant local time variations, seasonal dependencies, hemispheric asymmetries, and  
68 a strong dependence on solar activity. Grygalashvily et al. (2021) examined the semi-  
69 annual variation of the excited OH emission layer at mid-latitudes, attributing the  
70 results to the semi-annual oscillation of atomic oxygen and temperature.

71 Among the most prominent dynamical phenomena in the middle atmosphere are  
72 stratospheric sudden warmings (SSW), a large-scale wintertime phenomenon  
73 characterized by a rapid stratospheric temperature increase, zonal wind reversal, and  
74 substantial disruptions in atmospheric circulation (Manney et al., 2008; Chen et al.,  
75 2016; Bolaji et al., 2016; Gu et al., 2021). Studies have shown that SSW events are able  
76 to greatly modulate variations of atmospheric chemistry parameters (e.g., Kumar et al.  
77 2024), particularly OH concentration (e.g., Winick et al., 2009). For example, Winick  
78 et al. (2009) attributed variations in OH layer to concurrent changes in temperature and  
79 atomic oxygen concentration in the upper mesosphere during the winters of 2004 and  
80 2006. Similarly, Gao et al. (2011) documented reductions in OH and O<sub>2</sub> emissions  
81 associated with the January 2009 SSW, whereas Medvedeva et al. (2019) identified  
82 longitudinal disparities in OH emissions during the January 2013 SSW, which were  
83 likely modulated by variations in vertical wind patterns.

84 In certain cases, particularly following major SSW events, an elevated stratopause  
85 (ES) may form, marked by an anomalously large ascent in stratopause height (Manney  
86 et al., 2008; Limpasuvan et al., 2016). Unlike typical SSW events, ES-SSWs can induce  
87 stronger and longer-lasting disturbances that extend well into the MLT, leading to  
88 enhanced traveling planetary wave activity, altered thermal structures, and significant  
89 changes in mesospheric chemical composition, including OH concentration (Qin et al.,  
90 2024; Rhodes et al., 2021; Tweedy et al., 2013). Nevertheless, the investigations into  
91 the impacts of ES-SSWs on polar mesospheric chemistry remain limited due to the  
92 sparse sampling of satellite observations, as exemplified by the TIMED/SABER  
93 satellite, which follows a precession orbit and requires several days to achieve full local  
94 time coverage. As a result, the influences of ES-SSWs on polar mesospheric OH



95 concentration remain insufficiently understood.

96 Numerical simulations offer an alternative approach for investigating variations in  
97 the OH layer under dynamically complex conditions. The Specified Dynamics Whole  
98 Atmosphere Community Climate Model with ionosphere/thermosphere eXtension  
99 (SD-WACCM-X) offers a physically consistent representation of mesospheric  
100 chemistry and dynamics, allowing for a more continuous and spatially resolved analysis  
101 of OH layer responses to ES-SSW events. Previous studies have successfully employed  
102 SD-WACCM-X to investigate atmospheric dynamics procession (e.g., Zhang et al.,  
103 2025; Orsolini et al., 2022), which demonstrates that the SD-WACCM-X simulations  
104 provide a valuable opportunity for capturing OH variations during ES-SSWs in the  
105 absence of comprehensive observational coverage.

106 This study aims to explore the responses of OH concentrations to ES-SSW events  
107 using the SD-WACCM-X simulations for the period 2004–2023. Section 2 provides a  
108 brief introduction to the datasets, the definition of ES-SSW, and the analysis methods  
109 used in this study. Section 3 presents the results, focusing on the peak values and peak  
110 height of OH concentrations, along with their temporal evolution in response to ES-  
111 SSW events. Section 4 discusses the roles of mesospheric temperature and atomic  
112 oxygen in changes of OH layer and the underlying mechanisms of OH concentration  
113 variations during ES-SSW events. Finally, Section 5 summarizes the key findings and  
114 their implications for mesospheric dynamics during ES-SSWs.

115

## 116 **2. Data and Method**

### 117 **2.1 SD-WACCM-X**

118 In this study, the Whole Atmosphere Community Climate Model with  
119 ionosphere/thermosphere eXtension (WACCM-X), an extended version of WACCM  
120 embedded within the Community Earth System Model version 2 (CESM2) framework  
121 developed by the National Center for Atmospheric Research (NCAR) (e.g.,  
122 Danabasoglu et al., 2020; Yang et al., 2018; Yu et al., 2022; Sassi et al., 2018), is  
123 employed to consider the characteristics of OH layer in the polar mesosphere.  
124 WACCM-X is an atmospheric model that simulates atmospheric processes from the  
125 surface (~0 km) up to the ionosphere/thermosphere, extending to ~700 km depending



126 on solar activity, which provides a detailed representation of dynamic, chemical, and  
127 radiative processes in the stratosphere, mesosphere, and thermosphere. The WACCM-  
128 X used in this study is based on the Community Atmosphere Model-6 (CAM-6) physics  
129 and the three-dimensional chemical transport Model for Ozone and Related chemical  
130 Tracers (MOZART) chemistry (Gettelman et al., 2019). Specifically, WACCM-X  
131 incorporates nonorographic gravity wave drag parameterization, solar and geomagnetic  
132 forcing, and comprehensive gas and aerosol chemistry (Lee et al., 2021). The middle  
133 atmosphere scheme with the D-region chemistry (MAD) is used.

134 The specified dynamics (SD) configuration of WACCM-X is nudged by Modern-  
135 Era Retrospective Analysis for Research and Applications Version 2 (MERRA-2) data  
136 (e.g., Molod et al., 2015; Teng et al., 2021) to ensure consistency with observed  
137 meteorological conditions. Both chemical and dynamical parameters in SD-WACCM-  
138 X are relaxed toward linearly time-interpolated 3-hourly MERRA-2 reanalysis data.  
139 The relaxation coefficient is uniform below 50 km, decreases progressively above this  
140 altitude, and becomes zero above 60 km (Brakebusch et al., 2013). Consequently, the  
141 model is unconstrained by reanalysis above 60 km. The vertical resolution of the model  
142 ranges from ~1.1 km to ~3.5 km, with a vertical density of two points per scale height  
143 below ~50 km and increasing to four points per scale height above ~50 km (Salinas et  
144 al., 2023). Enhanced vertical resolution in the troposphere and stratosphere enables  
145 improved representation of key physical processes (Sassi and Liu, 2014). The  
146 horizontal resolution is typically set to  $1.9^{\circ} \times 2.5^{\circ}$  (latitude×longitude).

147 SD-WACCM-X simulations have been demonstrated to effectively reproduce  
148 observed atmospheric responses to ES-SSW events (e.g., Limpasuvan et al., 2015; Lee  
149 et al., 2021; Zhang et al., 2021; Zhang et al., 2025; Orsolini et al., 2022). These  
150 successes highlight the model's robustness in capturing the dynamical and chemical  
151 processes, particularly within the MLT. In this study, model outputs spanning the period  
152 from 2004 to 2023 are utilized, with data from December through March extracted for  
153 each year, corresponding to the climatological window during which ES-SSW events  
154 predominantly occur. To comprehensively elucidate the response of the OH layer on  
155 ES-SSW, key variables such as OH, atomic oxygen, temperature, zonal wind, and so  
156 on are output. From these outputs, daily means of relevant dynamical and chemical



parameters are derived to facilitate temporal-spatial evaluation of ES-SSW responses.

## 2.2 Definition of SSW and ES Events

An elevated stratopause (ES) event refers to a phenomenon in which the winter polar stratopause initially descends, then becomes indistinct, and eventually reforms at a much higher altitude than usual (Chandran et al., 2013). The newly reformed stratopause is displaced by more than 15 km compared to its original altitude (Torre et al., 2012). The stratopause height is defined as the altitude of maximum temperature within the 20-100 km vertical domain (Chandran et al., 2013). ES events are frequently observed in connection with major SSW events. According to the criteria established by the World Meteorological Organization (WMO), a major SSW is identified: at 10 hPa or below, the latitudinal mean temperature must increase poleward of 60° latitude, accompanied by a reversal in the zonal-mean zonal winds (i.e., a transition from mean westerly to mean easterly winds poleward of 60° latitude).

To develop a statistically robust understanding of OH layer characteristics during ES-SSW, a composite analysis is conducted by temporally aligning each event such that Day 0 corresponds to the onset, defined as the day when the eastward wind reverses to a westward wind at 50 km with the maximum reversed wind. This alignment allows for a systematic examination of the temporal evolution and spatial structure of OH layer during ES-SSW events, providing insights into their common features and variability. In this study, the response of OH layer to ES-SSW events is categorized into three distinct stages based on the temporal evolution of temperature: Day -15 to Day 0 is considered the normal stage; Day 0 to Day 5 correspond to the stratosphere warming stage; Day 6 to Day 60 correspond to the elevated stratopause stage.

## 3. Results

The SSW event that commenced in January 2009 started as the strongest, most prolonged on record, and isolated, which has been made a focal point for numerous studies (e.g., Manney et al., 2009; Yue et al., 2010; Limpasuvan et al., 2011). These unique characteristics render it particularly suitable for employing the response of mesospheric chemical composition to SSW events. The response of OH concentrations to ES-SSW events is exemplified by the 2009 SSW case, as illustrated in Figure 1. From

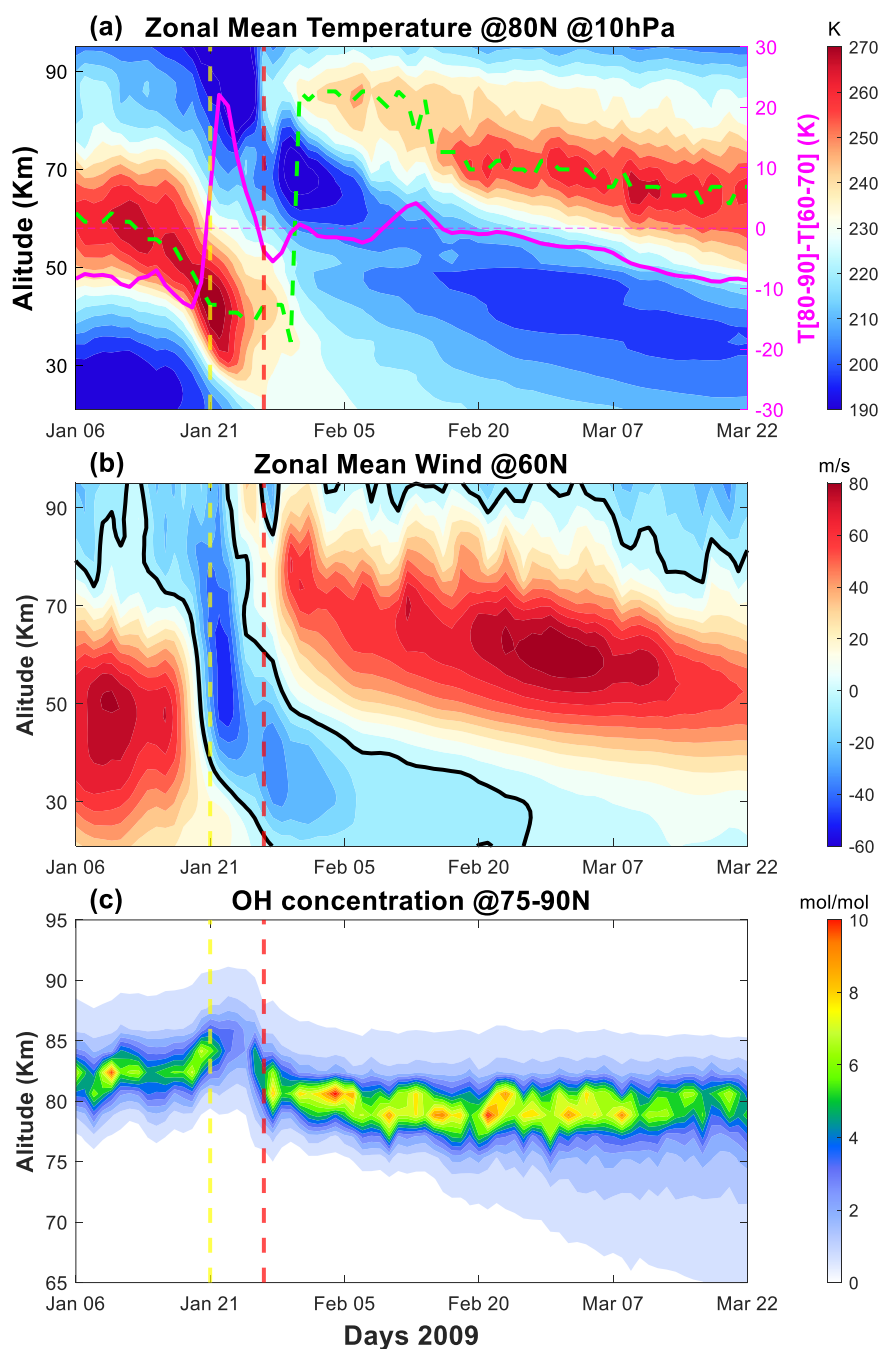


188 top to bottom, Figure 1 represents zonal-mean temperature at 10 hPa (~32 km) and 80°  
189 N, zonal-mean wind at 60° N, and temporal variations in OH concentrations at latitudes  
190 75~90° N from January 6, 2009, to March 22, 2009. In Figure 1a, the meridional  
191 temperature gradient ( $T[80^\circ - 90^\circ] - T[60^\circ - 70^\circ]$  K) is denoted by the pink solid line,  
192 and the height of the ES is indicated by the green dashed line.

193 Prior to January 10, 2009, the temperature peak is located at 61 km, with a  
194 maximum ~272 K. Subsequently, the peak height drops sharply, reaching ~37.7 km by  
195 January 21, 2009. Between January 21 and January 26, 2009, the minimum temperature  
196 of 183.5 K occurs at altitudes above 75 km, while the meridional temperature gradient  
197 at 10 hPa transitions to positive values. After January 26, 2009, a new stratopause forms  
198 at 86 km, with an upward displacement of 51 km compared to the stratopause altitude  
199 before January 10, 2009, and subsequently descends to its climatological altitude in  
200 conjunction with the recovery of the polar vortex (Limpasuvan et al., 2012). This  
201 elevated stratopause event is accompanied by a pronounced downwelling over the  
202 winter pole, extending from 45 to 95 km. The enhanced subsidence facilitates the  
203 downward transport of MLT air into the stratosphere, thereby modulating the thermal  
204 structure and influencing polar chemical processes.

205 Figure 1b depicts the zonal mean wind changes at 60° N. Before the SSW onset,  
206 the zonal mean wind is eastward with a speed of ~85 m/s. During the stratosphere  
207 warming phase, the zonal mean flow reverses to westward winds (below 0 m/s) in the  
208 polar winter stratosphere, confirming the occurrence of a major SSW event.  
209 Subsequently, the zonal-mean wind structure during the elevated stratopause exhibits a  
210 pattern similar to that of the zonal-mean temperature, with eastward winds prevailing  
211 in the mesosphere region at ~91.8 m/s. As the polar vortex recovers, the eastward wind  
212 gradually descends to its climatological distribution, mirroring the temperature  
213 evolution in the stratosphere and mesosphere.

214



215

216 **Figure 1.** Time-altitude cross-section of SD-WACCM-X zonal-mean (a) temperature  
217 at 80°N, (b) zonal wind at 60°N, and (c) OH concentration (in units of  $10^{-9}$ ) during





January 06–March 22, 2009. The solid pink line represents the meridional temperature gradient ( $T[80^\circ - 90^\circ] - T[60^\circ - 70^\circ]$ ), and the dashed green line is the stratopause height. The black solid contour in (b) denotes the zero-wind line. Vertical dashed yellow and red lines are the onset of the stratosphere warming stage and elevated stratopause stage, respectively.

Figure 1c illustrates the temporal variation of OH concentration in 2009. Prior to the SSW onset, the OH concentrations remain  $\sim 7.2 \times 10^{-9}$  mol/mol with a peak height  $\sim 82.4$  km. However, between January 21 and January 26, 2009, a pronounced depletion in OH concentrations is observed reaching a minimum of  $\sim 2.35 \times 10^{-9}$  mol/mol, while the peak altitude shifts upward to 86 km. Following January 26, 2009, the peak of OH concentrations exhibits a gradual increase, eventually surpassing the pre-SSW levels and reaching values of  $\sim 10.6 \times 10^{-9}$  mol/mol. This enhanced concentration persisted and did not return to its climatological level until March 9, 2009. These fluctuations align with findings from other studies (Gao et al., 2011; Winick et al., 2009).

**Table 1** Onset Day (Day 1 corresponds to January 1 of the Year) of the ES-SSW Events During 2004~2023

Years	Onset day	Years	Onset day
2003/2004	Jan 2	2012/2013	Jan 5
2005/2006	Jan 9	2017/2018	Feb 14
2008/2009	Jan 21	2018/2019	Dec 25
2009/2010	Jan 20	2020/2021	Jan 2
2011/2012	Jan 11	2022/2023	Feb 13

Note. ES-SSW, sudden stratosphere warming with elevated stratopause.

To further validate the observed response of OH concentrations to ES-SSW events, SSW occurrences from 2004 to 2023 are analyzed, aiming to identify common characteristics across multiple events. Based on the criteria outlined in the methodology section, a total of ten ES-SSW events are identified (Manney et al., 2008; Maute et al., 2014; Kodera et al., 2008; Manney et al., 2009; Harada et al., 2010; Jones et al., 2018; Chandran et al., 2013; Goncharenko et al., 2013; de Wit et al., 2014; Karpechko et al., 2018; Rao et al., 2019; Okui et al., 2021; Lu et al., 2021; Qin et al., 2024; Zhang et al., 2025), with their occurrence years and onset dates listed in Table 1. The left column of



the table indicates the years in which ES-SSW events occurred, while the right column specifies the first day of each event.

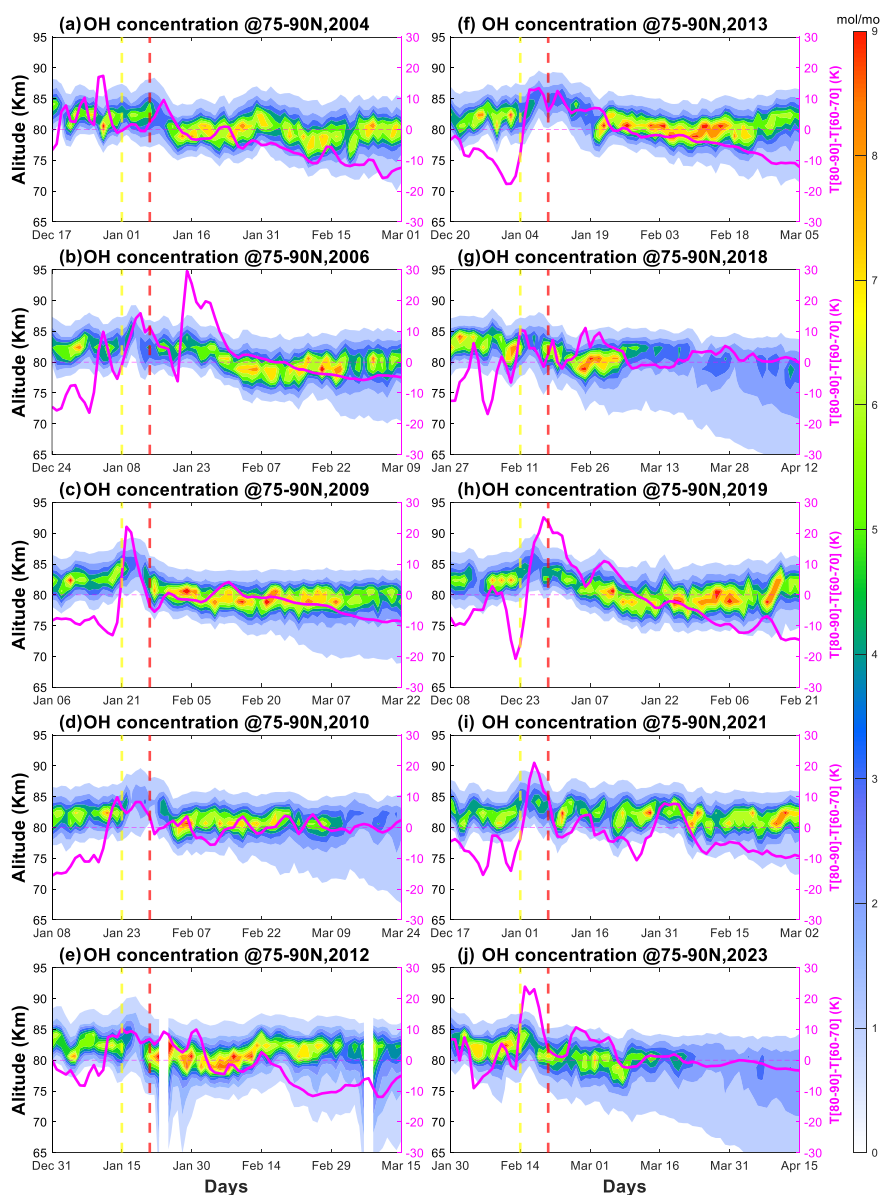


**Figure 2.** Time-altitude cross-sections of OH concentrations (in units of  $10^{-9}$ ) in ES-SSW events during 2004–2023 are captured in panels a–j. The solid pink line represents the meridional temperature gradient ( $T[80^{\circ}–90^{\circ}]–T[60^{\circ}–70^{\circ}]$ ). Vertical dashed yellow and red lines are the onset of the stratosphere warming stage and elevated



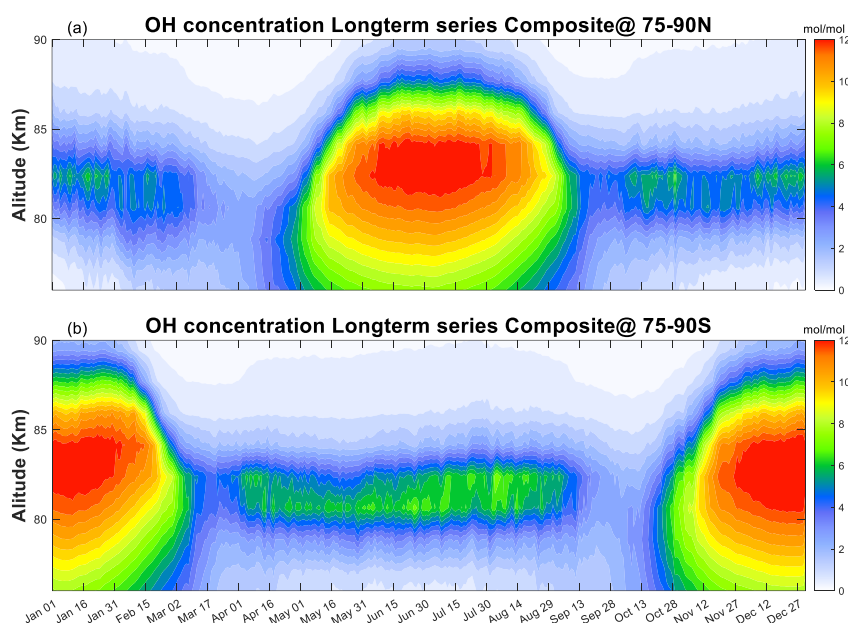
250 stratopause stage, respectively.

251 Figure 2 presents the temporal variations in OH concentrations for each selected  
252 year, centered on the onset day of the ES-SSW event and spanning from 15 days prior  
253 to 60 days after the onset. As shown, during the stratosphere warming phase, the peak  
254 height of OH concentration undergoes an evident upward displacement to ~86 km,  
255 whereas the OH concentrations peak experiences a sharp decline with the minimum of  
256  $\sim 1 \times 10^{-9}$ – $2 \times 10^{-9}$  mol/mol. Conversely, during the elevated stratopause phase, as the peak  
257 height of the OH layer significantly decreases, the peak OH concentration increases  
258 rapidly to  $\sim 7 \times 10^{-9}$ – $9 \times 10^{-9}$  mol/mol at 78 km, and its maximum is larger than that in the  
259 normal stage. The results reveal a consistent pattern similar to that shown in Figure 1c,  
260 demonstrating that the influence of ES-SSW events on OH concentration is a common  
261 feature across all identified occurrences. In certain years, i.e., 2010, 2018, and 2023,  
262 the influence of ES-SSW events on the structure of OH concentration appears weaker,  
263 potentially due to variations in event intensity or background atmospheric conditions.  
264 Furthermore, although SSW events vary in their duration and intensity, they tend to  
265 occur on an annual basis. Some events occur in close succession, as observed in 2008,  
266 whereas others appear as isolated episodes, such as the one in 2009. During ES-SSW  
267 events, preceding or subsequent SSW-related mesospheric warming and elevated  
268 stratopause phases remain active, introducing additional modulation to the observed  
269 OH variations.

270 Notably, OH concentrations in some major SSW events such as February 2010  
271 and 2023, also show a significant downward extension in altitude after March,  
272 suggesting that seasonal variability may play a noticeable role in the temporal evolution  
273 of OH concentrations. Figure 3 illustrates the seasonal evolution in OH concentrations  
274 in both the Northern and Southern Hemispheres. The OH concentration exhibits a clear  
275 seasonal pattern, with higher values in the summer hemisphere (May to August in the  
276 Northern Hemisphere; November to February in the Southern Hemisphere) and lower  
277 values in the winter hemisphere. The peak of OH concentration in the summer  
278 hemisphere reaches  $\sim 12.5 \times 10^{-9}$  mol/mol, whereas the minimum OH concentration in  
279 the winter hemisphere is  $\sim 5 \times 10^{-9}$  mol/mol. Additionally, the vertical distribution of OH  
280 concentration varies across different seasons. In the summer hemisphere, the OH



281 concentration extends over a broader altitude range, from ~75 km to ~87 km. In contrast,  
282 in the winter hemisphere, the OH peak is more confined, occurring at an altitude of  
283 ~82.5 km.



284  
285 **Figure 3.** Temporal evolution of OH concentration (in units of  $10^{-9}$ ) in the polar region,  
286 with the Northern Hemisphere in the top panel and the Southern Hemisphere in the  
287 bottom panel.

288 Figure 4 illustrates the composite evolution of zonal mean temperature, zonal  
289 mean wind, OH concentration, and anomaly OH concentration as functions of altitude  
290 and time. As depicted in Figures 4a and 4b, significant variations extend across nearly  
291 the entire altitude range. In the mesosphere, the zonal mean wind exhibits a rapid  
292 weakening of the eastward component around Day -8, then switches to westward after  
293 Day 0 with a minimum wind speed of around -27 m/s. Around Day 6, the eastward wind  
294 begins to intensify again, reaching a peak velocity exceeding 70 m/s near Day 40.  
295 Corresponding thermal changes accompany zonal wind reversal. At the onset of the ES-  
296 SSW event, the stratosphere undergoes rapid warming, leading to a sharp descent of the  
297 stratopause altitudes. As shown, until Day 3, the stratopause altitude reaches its lowest  
298 altitude of ~43.5 km, coinciding with the peak westward wind. The maximum  
299 temperature and wind speed are over 260 K and -27 m/s, respectively. After Day 6, as



300 the eastward wind begins to strengthen, a newly formed stratopause emerges near 80  
301 km.

302 The composite variabilities of OH concentrations and anomaly OH concentrations  
303 associated with ES-SSW events are examined, as shown in Figures 4c and 4d. Here, the  
304 composite results represent the mean structure aligning the temporal series of individual  
305 ES-SSW events. Figure 4c illustrates the temporal evolution of OH concentration. Prior  
306 to the onset of SSW, the peak of OH concentration exhibits a value of  $\sim 7.4 \times 10^{-9}$   
307 mol/mol, with a peak height near 82.4 km. During the stratosphere warming phase, the  
308 peak of OH concentration decreases to  $2.9 \times 10^{-9}$  mol/mol, while in the elevated  
309 stratopause phase, it increases to  $\sim 6.8 \times 10^{-9}$  mol/mol. In addition, the peak height of OH  
310 concentration rises by  $\sim 3.5$  km reaching  $\sim 85.9$  km during the warming phase, before  
311 descending by  $\sim 2$  km to  $\sim 80.6$  km during the elevated stratopause phase. This temporal  
312 evolution is consistent with that in 2009 shown in Figure 1. Winick et al. (2009)  
313 proposed that the anomalous characteristics of the OH layer may be associated with  
314 changes in the atomic oxygen concentration and temperature in the mesosphere, which  
315 is driven by the modification of polar circulation induced by ES-SSW events.

316 Similarly, the temporal evolutions are depicted in Figure 4d, which represents the  
317 variability of anomaly OH concentration (Anomaly = OH concentration – background  
318 average). The background averages of OH concentration are derived from the average  
319 of all aligned years from 2004 to 2023. As shown, during the stratosphere warming  
320 phase, the peak height of anomaly OH concentration occurs at 85.9 km with a maximum  
321 of  $\sim 1.3 \times 10^{-9}$  mol/mol. These situations in the elevated stratopause phase are  
322 significantly different. Compared to the stratosphere warming phase, the peak of  
323 anomaly OH concentration doubles, reaching a maximum of  $\sim 2.6 \times 10^{-9}$  mol/mol, while  
324 its peak height significantly decreases to 78.8 km. These phenomena again demonstrate  
325 the consistency between OH concentration enhancements/depletions and peak height  
326 descent/ascent, a relationship previously documented in J. R. Winick.

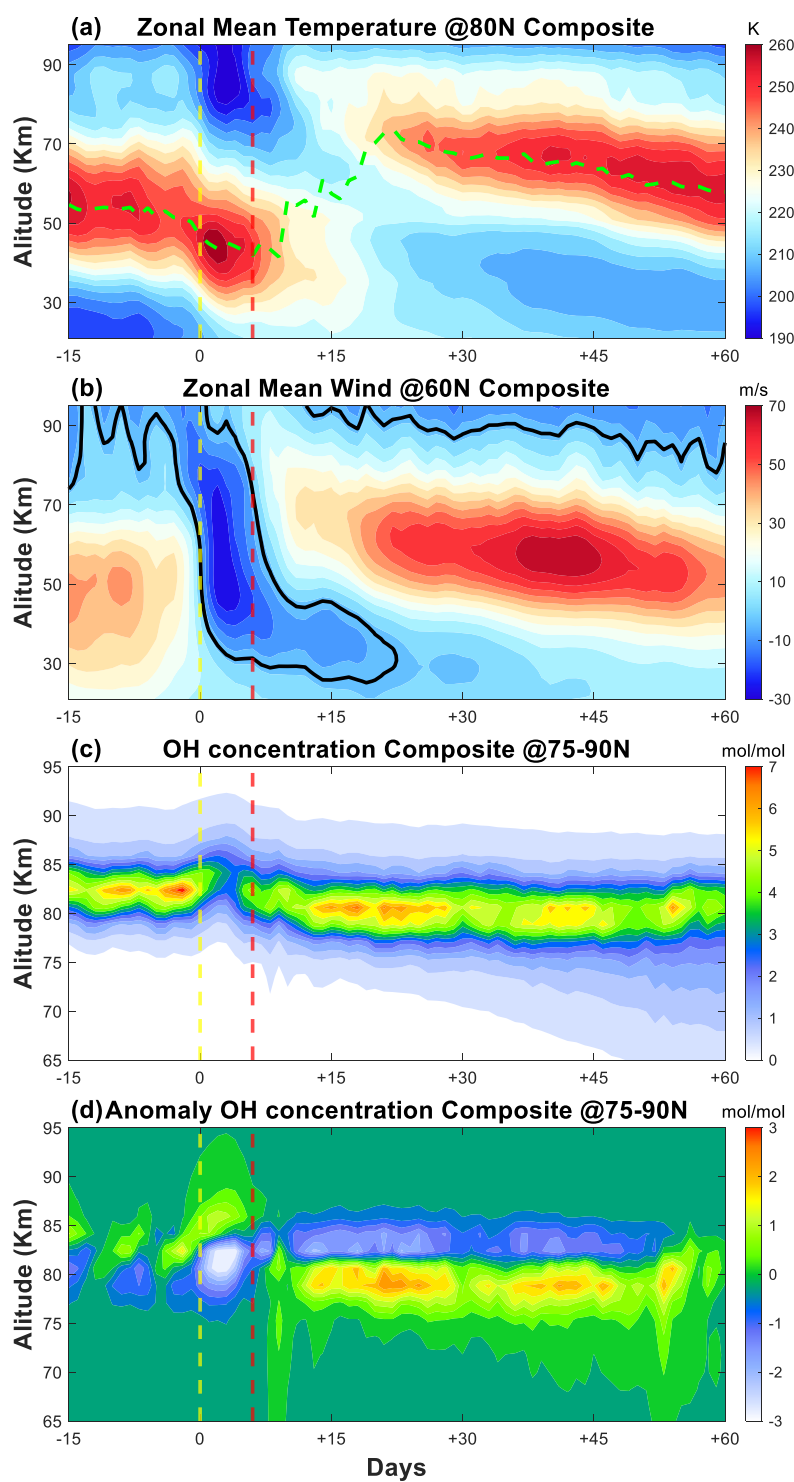


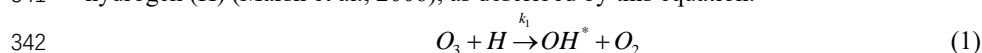


**Figure 4.** Time-altitude cross-section of composite zonal mean (a) temperature, (b) zonal wind, (c) OH concentration (in units of  $10^{-9}$ ), and (d) anomaly OH concentration. On the abscissa, time is relative to the ES-SSW onset (Day 0). Vertical dashed yellow and red lines are the onset of the stratosphere warming stage and elevated stratopause stage, respectively. The dashed green line is the stratopause height, while the black solid contour in (b) denotes the zero-wind line.

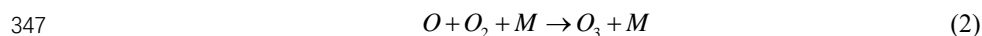
## 4. Discussion

### 4.1 Temporal variation

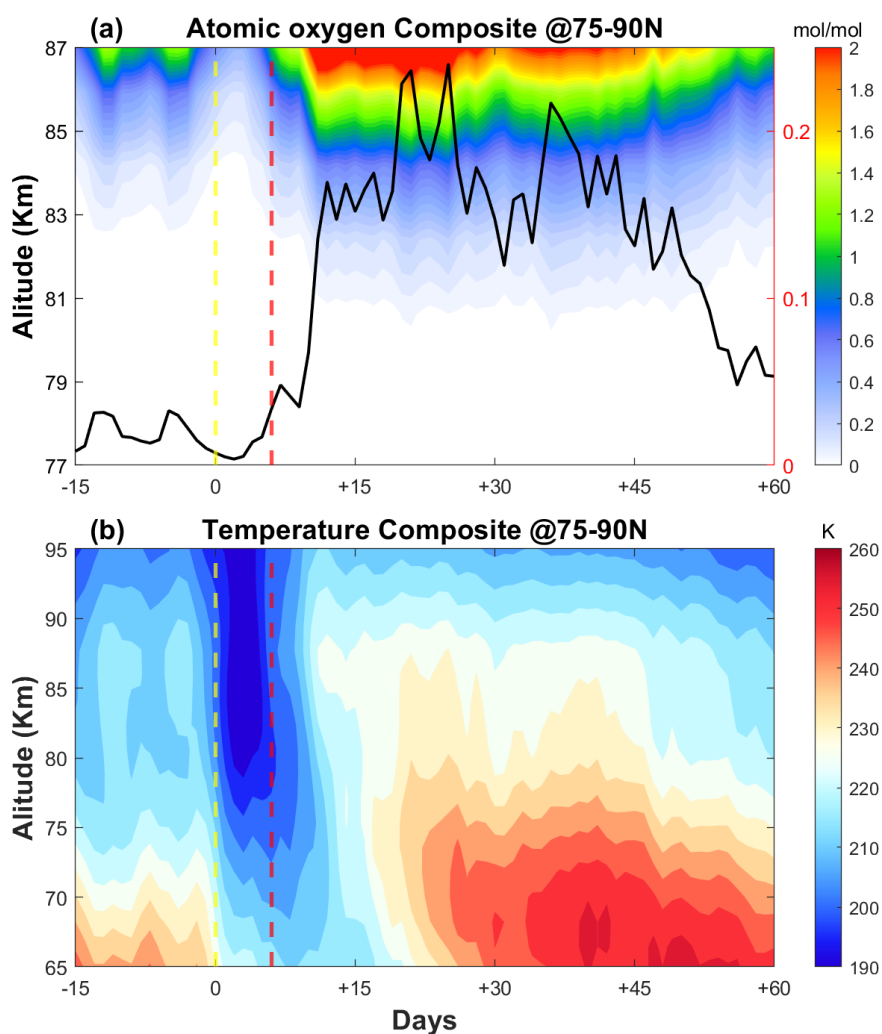
During the ES-SSW period, changes in atmospheric circulation lead to a strong descent/ascent motion of air at high latitudes. This dynamic change leads to subsequent increased/decreased atomic oxygen penetrating the mesopause. Within the mesospheric region, OH\* is primarily produced through the reaction between ozone ( $O_3$ ) and atomic hydrogen (H) (Marsh et al., 2006), as described by this equation:



According to Equation 1, the reaction rate coefficient  $k_1$  increases with temperature, thereby enhancing the efficiency of OH\* production. Ozone is formed through the reaction of atomic oxygen and molecular oxygen, as expressed in the equation:



Notably, this process,  $O + O_3 \rightarrow O_2 + O_2$ , also contributes to ozone destruction alongside OH\* production. However, below ~95 km, ozone loss due to its reaction with atomic hydrogen significantly exceeds that caused by atomic oxygen by several orders of magnitude (Xu et al., 2010). In addition, ozone can be considered to be in a steady state under nighttime conditions (i.e., polar winter), implying that the production of OH is proportional to atomic oxygen (Gao et al., 2011). This relationship indicates that the temporal evolution of OH concentration is strongly coupled with variations in atomic oxygen abundance and temperature in the mesopause.



356

357 **Figure 5.** Same as Figure 4, but for (a) atomic oxygen (in units of  $10^{-3}$ ) and (b)  
 358 temperature. The solid black line in (a) represents the temporal evolution of atomic  
 359 oxygen at 82 km.

360 Figure 5 presents the composite variations in atomic oxygen (Figure 5a) and  
 361 temperature (Figure 5b) over high latitudes (75°-90°N). In Figure 5a, the solid black  
 362 line illustrates the temporal evolution of atomic oxygen concentration at 82 km. The  
 363 atomic oxygen concentration increases with altitude in the mesopause. Since the atomic  
 364 oxygen concentration is relatively low at this level, the line plot is included to clearly





highlight its variation throughout the event. The temporal variations of OH (Figure 4c), atomic oxygen (Figure 5a), and temperature (Figure 5b) in the mesopause region exhibit a nearly synchronous evolution. During the stratosphere warming phase, the atomic oxygen concentration experiences a significant decline, with a minimum value of  $\sim 0.005 \times 10^{-3}$  mol/mol at 82 km, as indicated by the solid black line. Then, the atomic oxygen peak concentration remarkably increases, reaching a peak value of  $\sim 0.24 \times 10^{-3}$  mol/mol, which is substantially higher than the normal stage. Figure 5b displays the composite temperature variation, which closely corresponds to the evolution of atomic oxygen. The temperature minimum reaches its minimum ( $\sim 190$  K) during the stratosphere warming stage and peaks at  $\sim 260$  K in the elevated stratopause stage.

Figure 6 shows the relative temporal evolution of the vertical component of the

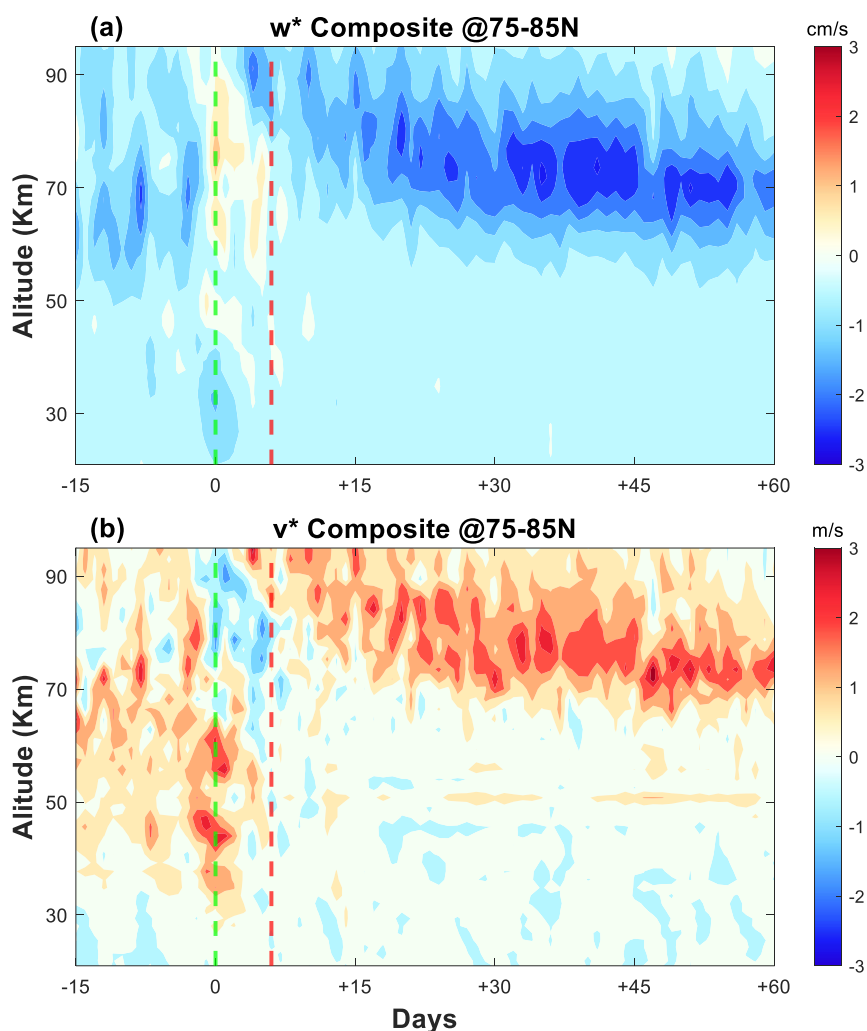
residual circulation (RC) ( $w^*$ ,  $w^* = \bar{w} + (a \cos \varphi)^{-1} (\cos \varphi \frac{\overline{v \theta}}{\bar{\theta}_z})_\varphi$ ) and the meridional

component of the residual circulation ( $v^*$ ,  $v^* = \bar{v} - \rho^{-1} (\rho \frac{\overline{v \theta}}{\bar{\theta}_z})_z$ ). During the

stratosphere warming phase, a strong downwelling (negative  $w^*$ ) develops in the stratosphere with a value of -1 cm/s, denoting enhanced adiabatic heating. Meanwhile, an anomalous upwelling (positive  $w^*$ ) emerges above  $\sim 70$  km in the mesosphere, peaking at  $\sim 1.4$  cm/s at  $\sim 77$  km, suggesting a weakening or even reversal of the climatological downward branch of the residual circulation over the winter polar cap (e.g., Gao et al., 2010; Limpasuvan et al., 2016). These vertical circulation anomalies directly modulate the mesospheric thermal structure: the upwelling leads to adiabatic cooling, consistent with the temperature decrease observed in Figure 4a, while the subsequent recovery of strong downwelling in the elevated stratopause phase (up to -2.5 cm/s) contributes to mesospheric warming. Additionally, the upwelling during the stratosphere warming phase lifts air with lower atomic oxygen concentrations into the mesopause, resulting in a significant depletion of atomic oxygen (Figure 5a). In contrast, enhanced downwelling during the elevated stratosphere phase brings oxygen-rich air



391 downward, increasing atomic oxygen concentration and thereby promoting OH  
392 production. During the stratosphere warming stage, an anomalous equatorward flow  
393 also emerges near the mesopause (Figure 6b), indicating a temporal reversal of the  
394 climatological poleward residual circulation. As the stratopause elevates, this  
395 meridional circulation returns to a poleward pattern. The reversal and recovery of  
396 meridional circulation could promote inter-latitudinal transport, potentially  
397 contributing to OH variations at lower latitudes, such as the equatorial region.



398

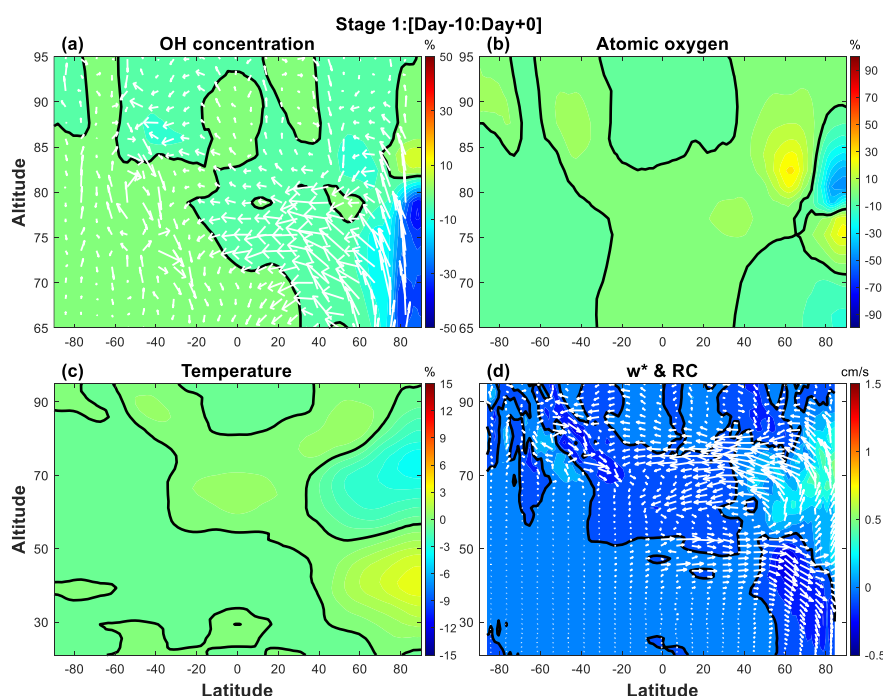
399 **Figure 6.** Same as Figure 4, but for (a)  $w^*$  and (b)  $v^*$ .



## 4.2 Spatial distribution

As shown in the preceding figures, the most prominent variations in OH concentration associated with ES-SSW event occur primarily within the first 30 days following the SSW onset, during which OH, atomic oxygen, temperature, and  $w^*$  exhibit substantial perturbations. To further investigate the meridional structure of these responses, the relative variations of these parameters are analyzed across three distinct stages: Stage 1 (Day -10 to Day 0), Stage 2 (Day 0 to Day 5), and Stage 3 (Day 6 to Day 26). Figures 7-9 present the corresponding spatial distributions of each parameter during these stages.

Figure 7 illustrates the ES-SSW-related parameters as functions of latitude and altitude in Stage 1. The spatial structure of OH concentration in the polar mesosphere is depicted in Figure 7a. A local maximum appears near ~83 km with an enhancement of 10% relative to the background average, whereas below 80 km, OH concentration exhibits a marked decrease, reaching a minimum of -35.7%. Figure 7b presents the situation of the atomic oxygen, which displays notable differences from OH. For instance, the enhancement shifts downward, with a peak of 25.4% located near ~75 km, while the minimum atomic oxygen concentration reaches -46.3% at ~81 km in the polar region. The corresponding temperature distribution (Figure 7c) reveals a warming in the polar stratosphere and cooling in the polar mesosphere with the magnitudes of approximately 3% and -3%, respectively. Figure 7d shows the  $w^*$ , which increases slightly to ~0.4 cm/s between ~65 and 83 km at high latitude. Simultaneously, the polar meridional circulation, as indicated by the white arrows, shifts equatorward in the mesosphere. Prior to the SSW onset, the circulation pattern is characterized by a pole-to-pole circulation from the summer hemisphere toward the winter hemisphere. Notably, slight variations in these parameters can be detected even prior to the onset of the ES-SSW event. This early-stage response may be attributed to the fact that ES-SSW perturbances tend to emerge in the mesosphere several days before becoming evident in the stratosphere (Gao et al., 2011), as also reflected by the temperature variations in Figure 4a.



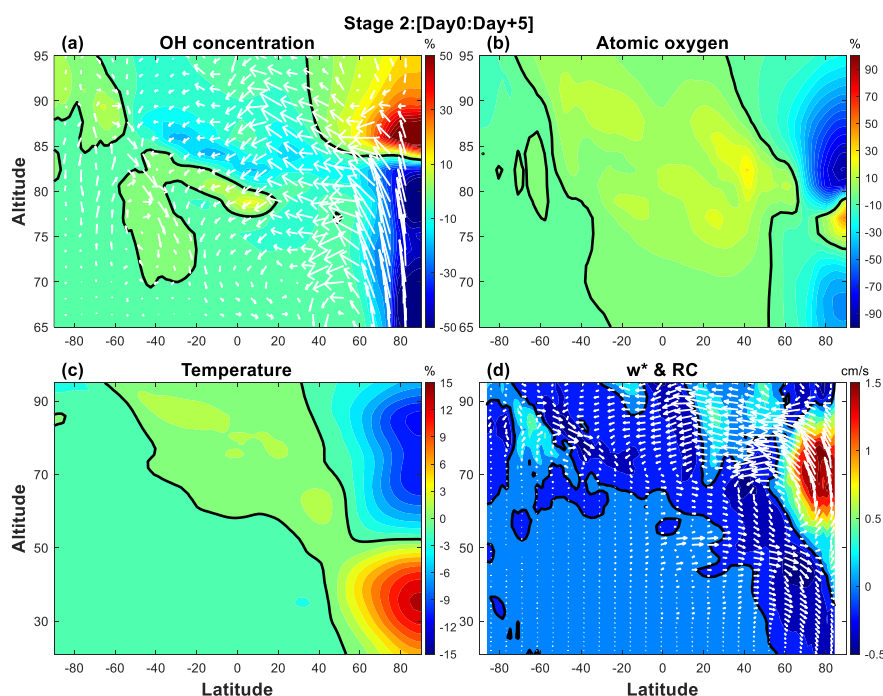
429

430 **Figure 7.** Latitude-altitude cross-sections of composite relative variation in (a) OH, (b)  
431 atomic oxygen, and (c) temperature, and composite absolute variation in (d)  $w^*$   
432 during Day -10 to Day 0 (Stage 1). The zero contour is denoted by a bold solid black  
433 line, white arrows represent the residual circulation.

434 Figure 8 illustrates the latitude-altitude structure of various elements in Stage 2,  
435 which exhibit significant responses to ES-SSW events. Compared to Stage 1, the OH  
436 concentration (Figure 8a) in the polar region displays a marked enhancement with a  
437 maximum increase of  $\sim 75.9\%$  relative to the background average occurring at  $\sim 85.9$   
438 km. Conversely, the minimum OH concentration reaches a pronounced decrease with  
439 an amplitude of  $-63.5\%$  at  $\sim 78.8$  km. The variations in atomic oxygen (in Figure 8b)  
440 are even more pronounced concerning Stage 2 over the latitudinal range of  $75^\circ$ - $90^\circ$ N,  
441 with a minimum reduction to  $-90.8\%$  and a maximum increase to  $\sim 48.3\%$  with respect  
442 to the background average. The temperature distribution in Figure 8c also reveals a  
443 noticeable response to the ES-SSW events, with a positive anomaly of  $13.9\%$  centered  
444 near 32 km and a negative anomaly of  $-11\%$  around 84 km in the polar region. Figure  
445 8d shows the spatial structure of  $w^*$  in Stage 2. Compared to Stage 1, the magnitude



446 of  $w^*$  in the polar mesosphere increases significantly, exceeding 1.78 cm/s between  
447  $\sim 64.6$  km and  $\sim 78.8$  km. These vertical structures are consistent with the findings of  
448 Dyrland et al. (2010) that associated OH airglow temperature perturbations with neutral  
449 atmospheric dynamics during the anomalous 2003-2004 winter. Their study also noted  
450 altitude-dependent evolution of the polar vortex.



451

452 **Figure 8.** Same as Figure 7, but for Day 0 to Day 5 (Stage 2).

453 In the present work, the intensified upward residual circulation at high northern  
454 latitudes is clearly observed, as indicated by the white arrows in Figure 8d. This upward  
455 motion turns equatorward in the upper mesosphere, forming a distinct pole-to-equator  
456 branch of the mesospheric circulation. Simultaneously, below  $\sim 50$  km, the poleward  
457 circulation exhibits a downward motion at the middle and high latitudes. The high-  
458 latitude downward circulation below  $\sim 50$  km and upward circulation above  $\sim 50$  km  
459 result in corresponding stratospheric warming and mesospheric cooling during the SSW  
460 period (as also shown in Figure 4a), respectively. Moreover, the upward transport of  
461 oxygen-poor air to higher latitudes, facilitated by enhanced residual circulation, results  
462 in a significant reduction in atomic oxygen concentrations. As a consequence, the peak



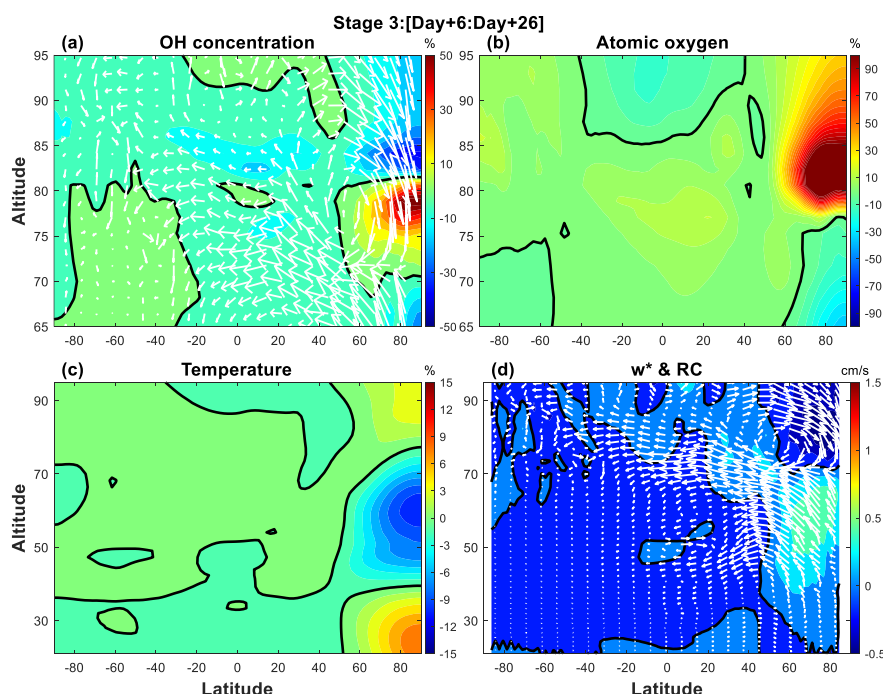
463 height of OH layer shifts upward, accompanied by a notable decrease in its peak  
464 concentration.

465 In addition, notable variations in OH concentration are also evident in the  
466 equatorial mesosphere region during Stage 2. Relative to the background average, a  
467 secondary OH peak appears at ~78.8 km with an amplitude of ~13.6%, while a local  
468 minimum of approximately -16.9% occurs at a higher altitude of ~82.4 km.  
469 Concurrently, both atomic oxygen and temperature exhibit modest enhancements in the  
470 equatorial mesosphere, with amplitudes of ~16% and ~1.5%, respectively. The  
471 observed temperature response in the equatorial region is consistent with that reported  
472 by Gu et al. (2009) in their analysis of the 2009 major SSW event (see their Figure 2e),  
473 which documented the middle atmospheric circulation response to SSW. However, the  
474 underlying dynamical and chemical mechanisms responsible for these compositional  
475 changes in the equatorial region remain unclear and warrant further investigation.

476 Figure 9 depicts the spatial distribution of multiple parameters during Stage 3,  
477 corresponding to Day 6 through Day 26 following the onset of the SSW. Compared to  
478 the preceding stages, the polar OH concentration structure undergoes a distinct reversal  
479 in vertical pattern. Specifically, the OH peak descends to ~78.8 km and intensifies to  
480 ~59.5%, while the minimum shifts to a higher altitude (~84.2 km) and weakens to  
481 negative 37.7%. As shown in Figure 9b, the atomic oxygen concentration exhibits a  
482 pronounced enhancement, with its peak occurring at ~82.4 km and exceeding 137.3%  
483 compared to the climatological average at high latitudes. The temperature field (Figure  
484 9c) displays a bifurcated structure, with a dominant warming centered around ~28 km  
485 with an amplitude of ~7.9% and a secondary weaker warming near the MLT region  
486 with a lower amplitude of ~3.7%. The vertical structure of the residual circulation  
487 (Figure 9d) also changes noticeably. The peak of  $w^*$  shifts downward to ~57 km with  
488 a reduced amplitude (~0.51 cm/s) in the polar region compared to earlier stages. As the  
489 mesospheric wind begins to eastward, the residual circulation transitions to a pole-to-  
490 pole pattern from the summer to winter hemisphere, and then descends vertically above  
491 ~70 km in the polar region. This downward motion facilitates the downward transport  
492 of oxygen-rich air into the polar mesopause region and warming around 80 km.  
493 Consequently, the OH concentration peak increases in magnitude while its altitude



494 decreases. In the equatorial region, the OH distribution in Stage 3 resembles that in  
495 Stage 2 but with reduced amplitude. The sustained presence of these anomalies may be  
496 attributed to continued enhancements in both atomic oxygen abundance and  
497 temperature in the equatorial region.



498  
499 Figure 9. Same as Figure 7, but for Day 6 to Day 26 (Stage 3).

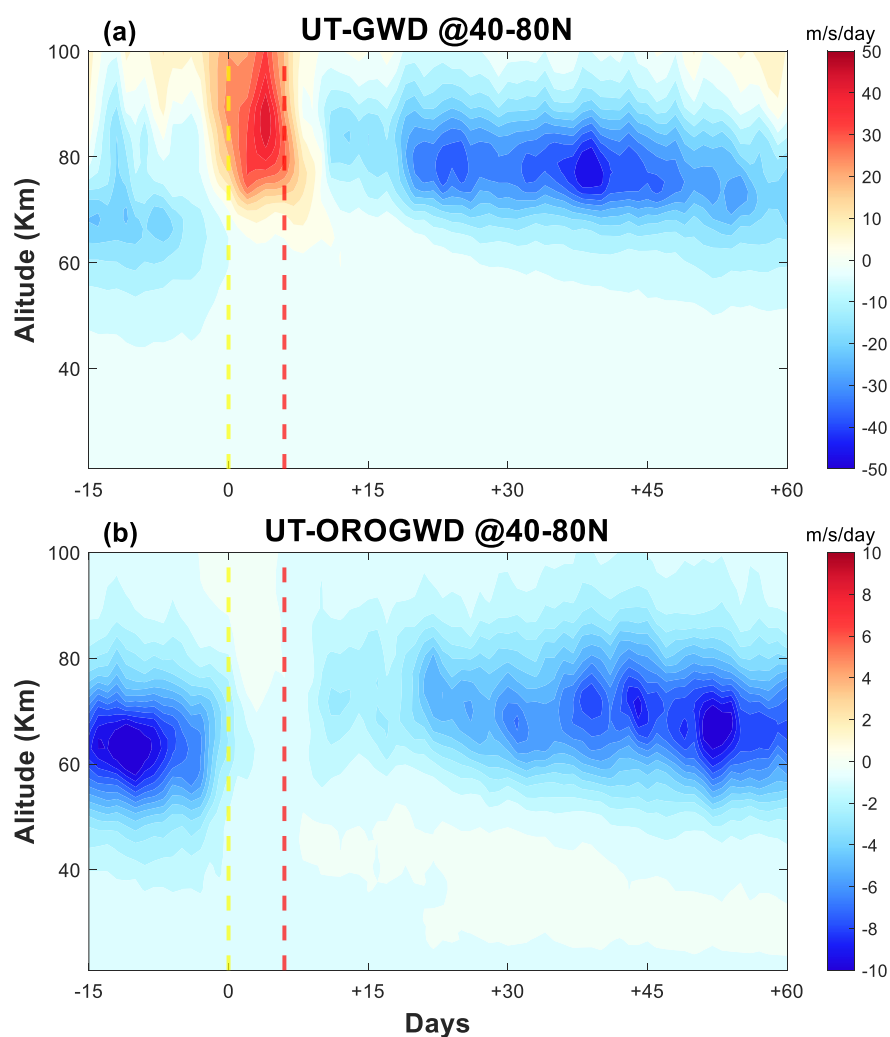
### 500 4.3 Potential mechanism

501 During SSW events, the reversal/deceleration of the stratospheric winter eastward  
502 wind due to planetary wave breaking allows more eastward-propagating GWs to  
503 penetrate into higher altitudes, enhancing upward and equatorward motion in the  
504 mesosphere. This altered circulation results in mesospheric cooling (Limpasuvan et al.,  
505 2012; Lukianova et al., 2015; Gu et al., 2020). The mesospheric OH layer variability  
506 may be dominantly controlled by changes in GWs during the ES-SSW events.

507 Figure 10 presents the temporal evolution of zonal wind tendency due to total  
508 gravity wave drag (GWD) and zonal wind tendency due to orographic gravity wave  
509 drag over the latitudes of 40°-80°N. Under the quiet conditions, westward GWs drag in  
510 the mesosphere sustains the polar circulation downwelling. As planetary wave activity  
511 intensifies, the weakening/reversal of the eastward jet starts in the mesosphere and



512 progresses to the stratosphere (Yang et al., 2024; Liu and Roble., 2005), with  
513 mesospheric changes preceding the stratospheric response by several days in Figure 4b  
514 (Gao et al., 2011; Coy et al., 2011; Kurihara et al., 2010; Azeem et al., 2005). Alteration  
515 of the wave transmission conditions enables eastward-propagating GWs to penetrate  
516 the mesosphere resulting in enhanced eastward GWD that modulates the mesospheric  
517 circulation (Figure 6) and induces a slight response in the polar OH layer (Figure 7a).



518

519 **Figure 10.** Time-altitude cross-section of SD-WACCM-X composite zonal mean (a)  
520 zonal wind tendency due to total gravity wave drag (UT-GWD) and (b) zonal wind





521 tendency due to orographic gravity wave drag (UT-OROGWD).

522       Following the stratosphere warming phase, a reversal of the zonal-mean wind from  
523 eastward to westward in the polar stratosphere and mesosphere is evident in Figure 4b.  
524 The stratospheric westward wind filters out westward phase speed components of GWs  
525 and facilitates the upward propagation of eastward-propagating GWs into the  
526 mesosphere, which results in anomalously eastward GWs exerting strong positive zonal  
527 wind tendency as shown in Figure 10a, peaking in the mesosphere around Day 4 with  
528 its maximum of 46.2 m/s/day. Enhanced eastward GWs forcing induces equatorward  
529 flow in the mesopause region and enhances the upward residual circulation extending  
530 from the stratosphere to the mesosphere at northern high latitudes, which can be seen  
531 vertical component and meridional component of residual circulation in Figures 6 and  
532 8d. This upward residual circulation transports oxygen-poor air upward, given that  
533 atomic oxygen concentration increases with altitude (seen in Figure 5a), leading to a  
534 reduction in atomic oxygen abundance in the upper atmosphere. As a result, the peak  
535 OH concentration exhibits a substantial decrease, while its corresponding peak altitude  
536 undergoes a pronounced upward shift.

537       During the elevated stratopause phase, the thermal relaxation rate in the upper  
538 mesosphere and lower stratosphere is approximately two to three times that of the lower  
539 stratosphere (Wehrbein et al., 1982; Chandran et al., 2014), promoting the rapid  
540 recovery of the polar eastward zonal wind (Hitchman et al., 1989). Consistent with the  
541 initial response to the disturbance, the recovery of eastward zonal winds first appears  
542 in the mesosphere and then progressively propagates downward into the stratosphere.  
543 The GWs with westward phase speeds are again able to propagate into the mesosphere  
544 and subsequently dissipate, inducing a pronounced negative zonal wind tendency with  
545 a peak value reaching  $\sim 45$  m/s/day exceeding the climatological average. Enhanced  
546 GW breaking at higher latitudes within the MLT region drives an intensified poleward  
547 and downward branch of the residual circulation, leading to the reformation of elevated  
548 stratopause at high latitudes, as shown in Figure 4a (Chandran et al., 2014). Compared  
549 to quiet conditions, where such circulation is largely confined below 50 km, the  
550 poleward and downward flow extends above 70 km in the elevated stratopause phase.  
551 This pronounced downward motion promotes the descent of dry mesospheric air



552 (Orsolini et al., 2010), which causes an exceptionally strong vertical transport of atomic  
553 oxygen into the mesopause region. Consequently, the OH concentration returns toward  
554 the climatological level, with the peak of OH layer occurring at a lower altitude.

555 Generally, GWs can be categorized into orographic and non-orographic  
556 components (Gilli et al., 2020; Richter et al., 2010). As shown in Figure 10b, the  
557 momentum deposition induced by orographic GWs is primarily confined to the altitude  
558 range of 40~80 km with values ranging from -10.5 to 0.5 m/s/day. During the  
559 stratosphere warming phase, orographic GWs are largely filtered and inhibited from  
560 upward propagation, leading to a notable reduction of their drag contribution (Liu et al.,  
561 2019). In the elevated stratopause phase, the zonal wind tendency associated with  
562 orographic GWD shows a different vertical structure compared to that associated with  
563 total GWD (see Figure 10a), particularly exhibiting a less significant enhancement at  
564 higher altitudes. It is demonstrated that orographically generated GWs play a secondary  
565 role in the overall momentum budget relative to non-orographic GWs. Non-orographic  
566 GWs, which are parameterized mainly from frontogenesis and convection sources (Holt  
567 et al., 2017), dominate the momentum deposition in the mesospheric polar region  
568 during ES-SSW events. The contribution from convective GWs is comparatively  
569 negligible, while frontogenetical generated GWs emerge as the primary source of GWs  
570 drag (Limpasuvan et al., 2012, 2016). Given the dominant role of frontogenesis GWs  
571 in driving mesospheric dynamics during ES-SSW events, it is suggested that the  
572 variability observed in the OH layer is predominantly modulated by gravity wave  
573 activity associated with frontogenesis.

574

## 575 **5 Conclusions**

576 In this paper, the responses of the peak concentration and peak height changes in  
577 the polar OH layer to ES-SSW events in the mesosphere are investigated based on SD-  
578 WACCM-X simulations. By compositing ten ES-SSW events from 2004 to 2023,  
579 distinct variations in OH layer structure associated with different phases of these events  
580 are revealed. The results demonstrate that the anomalous behaviors of the OH  
581 concentrations are closely synchronous with changes in mesospheric temperature,  
582 atomic oxygen concentrations, and the vertical component of the residual circulation in



583 the MLT region. GWs play a pivotal role by altering the vertical motion of circulation  
584 in the MLT region, which modulates the zonal wind and temperature fields. The  
585 enhanced downward/upward motion driven by GWs leads to mesospheric  
586 warming/cooling and an increase/decrease in atomic oxygen, which facilitates an  
587 increase/decrease in OH concentration.

588 The impact of ES-SSW extends well from the polar to the equator, strongly  
589 altering the zonal-mean zonal wind, temperature, and atomic oxygen distribution.  
590 However, the response of the mesopause OH layer in the equatorial region to ES-SSW  
591 is unclear. Our study enhances the understanding of OH layer responses to stratospheric  
592 perturbations and provides new insights into vertical coupling processes in the middle  
593 and upper atmosphere. Future research should focus on quantifying the relative  
594 contributions of these factors and assessing their implications for long-term  
595 atmospheric dynamics and chemistry.

596

#### 597 **Data availability.**

598 WACCM-X is an open-source software with source code publicly available at  
599 [https://escomp.github.io/CESM/release-](https://escomp.github.io/CESM/release-cesm2/downloading_cesm.html#downloading-the-code-and-scripts)  
600 [cesm2/downloading\\_cesm.html#downloading-the-code-and-scripts](https://escomp.github.io/CESM/release-cesm2/downloading_cesm.html#downloading-the-code-and-scripts). The atmospheric  
601 forcing data, which are regridded from the MERRA-2 data set and used to run  
602 WACCM-X, can be downloaded at <https://rda.ucar.edu/datasets/ds313.3/?hash=access>.  
603 For access to the SD-WACCM-X simulation data, please contact the corresponding  
604 authors: Sheng-yang Gu (gushengyang@whu.edu.cn) or Yusong Qin  
605 (qinyusong@whu.edu.cn).

606

607 **Author contribution.** Conceptualization and investigation were conducted by Jin Hu.  
608 Formal analysis and visualization were performed by Jin Hu with guidance and  
609 supervision from Sheng-yang Gu and Yusong Qin. Data curation for SD-WACCM-X  
610 was carried out by Yuxuan Liu. All authors contributed to the discussion of results and  
611 the revision of the manuscript.

612

613 **Competing interests.** The contact author has declared that none of the authors has any



614 competing interests.

615

616 **Acknowledgments.** The authors acknowledge the National Center for Atmospheric  
617 Research (NCAR) for providing the SD-WACCM-X model simulations and NASA for  
618 supplying the MERRA-2 reanalysis data.

619

620 **Financial support.** This research was supported by the National Natural Science  
621 Foundation of China (Grant Numbers 42374195 and 42404168), the fellowship of  
622 China National Postdoctoral Program for Innovative Talents (Grant Number  
623 BX20230273), the Hubei Provincial Natural Science Foundation of China (Grant  
624 Number 2024AFB097), and the Postdoctor Project of Hubei Province (Grant Number  
625 2024HBBHCXA054).

626

627

## 628 **Reference**

629 Azeem, S. I., E. R. Talaat, G. Sivjee, H.-L. Liu, and R. G. Roble (2005). Observational  
630 study of the 4-day wave in the mesosphere preceding the sudden stratospheric  
631 warming events during 1995 and 2002, *Geophys. Res. Lett.*, 32, L15,804,  
632 doi:10.1029/2005GL023393.

633 Bolaji, O. S., et al. (2016). Solar quiet current response in the African sector due to a  
634 2009 sudden stratospheric warming event, *J. Geophys. Res. Space Physics*, 121,  
635 doi:10.1002/2016JA022857

636 Brakebusch, M., C. E. Randall, D. E. Kinnison, S. Tilmes, M. L. Santee, and G. L.  
637 Manney (2013). Evaluation of Whole Atmosphere Community Climate Model  
638 simulations of ozone during Arctic winter 2004–2005, *J. Geophys. Res. Atmos.*,  
639 118, 2673–2688, doi:10.1002/jgrd.50226

640 Chandran, A., Collins, R. L., Garcia, R. R., Marsh, D. R., Harvey, V. L., Yue, J., and L.  
641 de la Torre (2013). A climatology of elevated stratopause events in the whole  
642 atmosphere community climate model, *J. Geophys. Res. Atmos.*, 118, 1234–1246,  
643 doi:10.1002/jgrd.50123.

644 Chandran, A., Collins, R. L., & Harvey, V. L. (2014). Stratosphere-mesosphere



- 645 coupling during stratospheric sudden warming events. *Advances in Space*  
646 *Research*, 53(9), 1265–1289.
- 647 Chen, G., Wu, C., Zhang, S., Ning, B., Huang, X., Zhong D., Qi H., Wang J., and Huang,  
648 L. (2016). Midlatitude ionospheric responses to the 2013 SSW under high solar  
649 activity, *J. Geophys. Res. Space Physics*, 121, 790–803, doi:10.1002/  
650 2015JA021980
- 651 Coy, L., S. D. Eckermann, K. W. Hoppel, and F. Sassi (2011), Mesospheric precursors  
652 to the major stratospheric sudden warming of 2009: Validation and dynamical  
653 attribution using a ground-to-edge-of-space data assimilation system, *J. Adv. Mod.*  
654 *Earth Syst.*, 3, M10,002, doi: 10.1029/2011MS000067.
- 655 Damiani, A., Storini, M., Santee, M. L., and Wang, S. (2010). Variability of the  
656 nighttime OH layer and mesospheric ozone at high latitudes during northern  
657 winter: influence of meteorology, *Atmos. Chem. Phys.*, 10, 10291–10303,  
658 <https://doi.org/10.5194/acp-10-10291-2010>, 2010.
- 659 Danabasoglu, G., Lamarque, J.-F., Bacmeister, J., Bailey, D. A., DuVivier, A. K.,  
660 Edwards, J., et al. (2020). The Community Earth System Model Version 2  
661 (CESM2). *Journal of Advances in Modeling Earth Systems*, 12, e2019MS001916.  
662 <https://doi.org/10.1029/2019MS001916>
- 663 de Wit, R. J., Hibbins, R., Espy, P. J., Orsolini, Y., Limpasuvan, V., & Kinnison, D. E.  
664 (2014). Observations of gravity wave forcing of the mesopause region during the  
665 January 2013 major sudden stratospheric warming. *Geophysical Research Letters*,  
666 41(13), 4745–4752. <https://doi.org/10.1002/2014GL060501>
- 667 Gao, H., Xu, J., and Chen, G.-M. (2016). The responses of the nightglow emissions  
668 observed by the TIMED/SABER satellite to solar radiation, *J. Geophys. Res.*  
669 *Space Physics*, 121, 1627–1642, doi:10.1002/2015JA021624.
- 670 Gao, H., Xu, J., and Q. Wu (2010). Seasonal and QBO variations in the OH nightglow  
671 emission observed by TIMED/ SABER, *J. Geophys. Res.*, 115, A06313,  
672 doi:10.1029/2009JA014641.
- 673 Gao, H., Xu, J., Ward, W., and A. K. Smith (2011). Temporal evolution of nightglow  
674 emission responses to SSW events observed by TIMED/SABER, *J. Geophys. Res.*,  
675 116, D19110, doi:10.1029/2011JD015936.



- 676 Gettelman, A., Mills, M. J., Kinnison, D. E., Garcia, R. R., Smith, A. K., Marsh, D. R.,  
677 et al. (2019). The Whole Atmosphere Community Climate Model Version 6  
678 (WACCM6). *Journal of Geophysical Research: Atmospheres*, 124(23), 12380–  
679 12403. <https://doi.org/10.1029/2019JD030943>
- 680 Gilli, G., Forget, F., Spiga, A., Navarro, T., Millour, E., Montabone, L., et al. (2020).  
681 Impact of gravity waves on the middle atmosphere of Mars: A non-orographic  
682 gravity wave parameterization based on global climate modeling and MCS  
683 observations. *Journal of Geophysical Research: Planets*, 125, e2018JE005873.  
684 <https://doi.org/10.1029/2018JE005873>
- 685 Goncharenko, L., Chau, J., Condor, P., Coster, A., & Benkevitch, L. (2013). Ionospheric  
686 effects of sudden stratospheric warming during moderate-to-high solar activity:  
687 Case study of January 2013. *Geophysical Research Letters*, 40(19), 4982–4986.  
688 <https://doi.org/10.1002/grl.50980>
- 689 Grygalashvily, M., Pogoreltsev, A. I., Andreyev, A. B., Smyshlyaev, S. P., and  
690 Sonnemann, G. R. (2021). Semi-annual variation of excited hydroxyl emission at  
691 mid-latitudes, *Ann. Geophys.*, 39, 255–265, [https://doi.org/10.5194/angeo-39-](https://doi.org/10.5194/angeo-39-255-2021)  
692 255-2021.
- 693 Gu, S.-Y., Teng, C.-K.-M., Li, N., Jia, M., Li, G., Xie, H., et al. (2021). Multivariate  
694 analysis on the ionospheric responses to planetary waves during the 2019 Antarctic  
695 SSW event. *Journal of Geophysical Research: Space Physics*, 126,  
696 e2020JA028588. <https://doi.org/10.1029/2020JA028588>
- 697 Harada, Y., Goto, A., Hasegawa, H., Fujikawa, N., Naoe, H., & Hirooka, T. (2010). A  
698 major stratospheric sudden warming event in January 2009. *Journal of the*  
699 *Atmospheric Sciences*, 67(6), 2052–2069. <https://doi.org/10.1175/2009JAS3320.1>
- 700 Hitchman, M. H., J. C. Gille, C. D. Rodgers, and G. Brasseur (1989), The separated  
701 polar winter stratopause: A gravity wave driven climatological feature, *J. Atmos.*  
702 *Sci.*, 46, 4310–422.
- 703 Holt, L. A., Alexander, M. J., Coy, L., Liu, C., Molod, A., Putman, W., & Pawson, S.  
704 (2017). An evaluation of gravity waves and gravity wave sources in the Southern  
705 Hemisphere in a 7 km global climate simulation. *Quarterly Journal of the Royal*  
706 *Meteorological Society*, 143(707), 2481–2495.



- 707 Holton, J. R. (1983). The influence of gravity wave breaking on the general circulation  
708 of the middle atmosphere, *J. Atmos. Sci.*, 40, 2497–2507.
- 709 Jones, M., Jr., Drob, D.P., Siskind, D.E., McCormack, J.P., Maute, A., McDonald, S.E.,  
710 & Dymond, K.F. (2018). Evaluating different techniques for constraining lower  
711 atmospheric variability in an upper atmosphere general circulation model: A case  
712 study during the 2010 sudden stratospheric warming. *Journal of Advances in*  
713 *Modeling Earth Systems*, 10(12),3076–3102.  
714 <https://doi.org/10.1029/2018MS001440>
- 715 Karpechko, A.Y., Charlton-Perez, A., Balmaseda, M., Tyrrell, N., & Vitart, F. (2018).  
716 Predicting sudden stratospheric warming 2018 and its climate impacts with a  
717 multimodel ensemble. *Geophysical Research Letters*, 45(24),13–538.  
718 <https://doi.org/10.1029/2018GL081091>
- 719 Kodera, K., Mukougawa, H., & Itoh, S. (2008). Tropospheric impact of reflected  
720 planetary waves from the stratosphere. *Geophysical Research Letters*, 35(16).  
721 <https://doi.org/10.1029/2008GL034575>
- 722 Kumar, A., Sunil Krishna, M. V., and Ranjan, A. K. (2024). Effect of 2009 major SSW  
723 event on the mesospheric CO<sub>2</sub> cooling. *Journal of Geophysical Research:*  
724 *Atmospheres*, 129, e2024JD041298. <https://doi.org/10.1029/2024JD041298>
- 725 Kurihara, J., Y. Ogawa, S. Oyama, S. Nozawa, M. Tsutsumi, C. M. Hall, Y. Tomikawa,  
726 and R. Fujii 2010, Links between a stratospheric sudden warming and thermal  
727 structures and dynamics in the high-latitude mesosphere, lower thermosphere, and  
728 ionosphere, *Geophys. Res. Lett.*, 37, L13806, doi: 10.1029/2010GL043643.
- 729 Lee, W., Song, I.-S., Kim, J.-H., Kim, Y. H., Jeong, S.-H., Eswaraiiah, S., and Murphy,  
730 D. J. (2021). The observation and SD-WACCM simulation of planetary wave  
731 activity in the middle atmosphere during the 2019 Southern Hemispheric sudden  
732 stratospheric warming. *Journal of Geophysical Research: Space Physics*, 126,  
733 e2020JA029094. <https://doi.org/10.1029/2020JA029094>
- 734 Li, K.-F., R. P. Cageao, E. M. Karpilovsky, F. P. Mills, Y. L. Yung, J. S. Margolis, and  
735 S. P. Sander (2005). OH column abundance over Table Mountain Facility,  
736 California: AM-PM diurnal asymmetry, *Geophys. Res. Lett.*, 32, L13813,  
737 doi:10.1029/2005GL022521.



- 738 Limpasuvan, V., M. J. Alexander, Y. J. Orsolini, D. L. Wu, M. Xue, J. H. Richter, and  
739 C. Yamashita (2011). Mesoscale simulations of gravity waves during the 2008–  
740 2009 major stratospheric sudden warming, *J. Geophys. Res.*, 116, D17104,  
741 doi:10.1029/2010JD015190.
- 742 Limpasuvan, V., Orsolini, Y. J., Chandran, A., Garcia, R. R., and Smith, A. K. (2016).  
743 On the composite response of the MLT to major sudden stratospheric warming  
744 events with elevated stratopause, *J. Geophys. Res. Atmos.*, 121, 4518–4537,  
745 doi:10.1002/2015JD024401.
- 746 Liu, H.-L., and R. G. Roble (2005). Dynamical coupling of the stratosphere and  
747 mesosphere in the 2002 Southern Hemisphere major stratospheric sudden  
748 warming, *Geophys. Res. Lett.*, 32, L13,804, doi: 10.1029/2005GL022939.
- 749 Liu, X., Xu, J., Yue, J., Vadas, S. L., & Becker, E. (2019). Orographic primary and  
750 secondary gravity waves in the middle atmosphere from 16-year SABER  
751 observations. *Geophysical Research Letters*, 46(8), 4512–4522.
- 752 Lu, Q., Rao, J., Liang, Z., Guo, D., Luo, J., Liu, S., et al. (2021). The sudden  
753 stratospheric warming in January 2021. *Environmental Research Letters*,  
754 16(8), 084029. <https://doi.org/10.1088/1748-9326/ac12f4>
- 755 Lukianova, R., A. Kozlovsky, S. Shalimov, T. Ulich, and M. Lester (2015), Thermal  
756 and dynamical perturbations in the winter polar mesosphere-lower thermosphere  
757 region associated with sudden stratospheric warmings under conditions of low  
758 solar activity, *J. Geophys. Res. Space Physics*, 120, 5226–5240,  
759 doi:10.1002/2015JA021269.
- 760 Manney, G. L., et al. (2008). The evolution of the stratopause during the 2006 major  
761 warming: Satellite data and assimilated meteorological analyses, *J. Geophys. Res.*,  
762 113, D11115, doi:10.1029/2007JD009097.
- 763 Manney, G. L., M. J. Schwartz, K. Krüger, M. L. Santee, S. Pawson, J. N. Lee, W. H.  
764 Daffer, R. A. Fuller, and N. J. Livesey (2009). Aura Microwave Limb Sounder  
765 observations of dynamics and transport during the record-breaking 2009 Arctic  
766 stratospheric major warming, *Geophys. Res. Lett.*, 36, L12815,  
767 doi:10.1029/2009GL038586.
- 768 Marsh, D. R., A. K. Smith, M. G. Mlynczak, and J. M. Russell III (2006). SABER





- 769 observations of the OH Meinel airglow variability near the mesopause, *J. Geophys.*  
770 *Res.*, 111, A10S05, doi:10.1029/2005JA011451
- 771 Maute, A., Hagan, M., Richmond, A., & Roble, R. (2014). TIME-GCM study of the  
772 ionospheric equatorial vertical drift changes during the 2006 stratospheric sudden  
773 warming. *Journal of Geophysical Research: Space Physics*, 119(2), 1287–1305.  
774 <https://doi.org/10.1002/2013JA019490>
- 775 Medvedeva I V, Semenov A I, Pogoreltsev A I, et al. (2019). Influence of sudden  
776 stratospheric warming on the mesosphere/lower thermosphere from the hydroxyl  
777 emission observations and numerical simulations[J]. *Journal of Atmospheric and*  
778 *Solar-Terrestrial Physics*, 2019, 187: 22-32.
- 779 Minschwaner, K., Manney, G. L., Wang, S. H., and Harwood, R. S. (2011). Hydroxyl  
780 in the stratosphere and mesosphere – Part 1: Diurnal variability, *Atmos. Chem.*  
781 *Phys.*, 11, 955–962, <https://doi.org/10.5194/acp-11-955-2011>.
- 782 Molod, A., Takacs, L., Suarez, M., and Bacmeister, J. (2015). Development of the  
783 GEOS-5 atmospheric general circulation model: Evolution from MERRA to  
784 MERRA2. *Geoscientific Model Development*, 8(5), 1339–1356.  
785 <https://doi.org/10.5194/GMD-8-1339-2015>
- 786 Okui, H., Sato, K., Koshin, D., & Watanabe, S. (2021). Formation of a mesospheric  
787 inversion layer and the subsequent elevated stratopause associated with the major  
788 stratospheric sudden warming in 2018/19. *Journal of Geophysical Research:*  
789 *Atmospheres*, 126(18), e2021JD034681. <https://doi.org/10.1029/2021JD034681>
- 790 Orsolini, Y. J., J. Urban, D. P. Murtagh, S. Lossow, and V. Limpasuvan (2010), Descent  
791 from the polar mesosphere and anomalously high stratopause observed in 8 years  
792 of water vapor and temperature satellite observations by the Odin SubMillimeter  
793 Radiometer, *J. Geophys. Res.*, 115, D12305, doi:10.1029/2009JD013501.
- 794 Orsolini, Y. J., Zhang, J., and Limpasuvan, V. (2022). Abrupt change in the lower  
795 thermospheric mean meridional circulation during sudden stratospheric warmings  
796 and its impact on trace species. *Journal of Geophysical Research: Atmospheres*,  
797 127, e2022JD037050. <https://doi.org/10.1029/2022JD037050>
- 798 Qin, Y., Gu, S.-Y., Dou, X., and Wei, Y. (2024). Unexpected global structure of quasi-  
799 4-day wave with westward zonal wavenumber 2 during the February 2023 unusual



- major sudden stratospheric warming with elevated stratopause. *Geophysical Research Letters*, 51, e2024GL109682. <https://doi.org/10.1029/2024GL109682>
- Rao, J., Garfinkel, C.I., Chen, H., & White, I.P. (2019). The 2019 new year stratospheric sudden warming and its real-time predictions in multiple S2S models. *Journal of Geophysical Research: Atmospheres*, 124(21), 11155–11174. <https://doi.org/10.1029/2019JD030826>
- Rhodes, C. T., Limpasuvan, V., and Orsolini, Y. J. (2021). Eastward-propagating planetary waves prior to the January 2009 sudden stratospheric warming. *Journal of Geophysical Research: Atmospheres*, 126, e2020JD033696. <https://doi.org/10.1029/2020JD033696>
- Richter, J. H., F. Sassi, and R. R. Garcia (2010), Toward a physically based gravity wave source parameterization in a general circulation model, *J. Atmos. Sci.*, 67, 136–156, doi:10.1175/2009JAS3112.1.
- Salinas, C. C. J. H., Wu, D. L., Lee, J. N., Chang, L. C., Qian, L., and Liu, H. (2023). Aura/MLS observes and SD-WACCM-X simulates the seasonality, quasi-biennial oscillation and El Niño–Southern Oscillation of the migrating diurnal tide driving upper mesospheric CO primarily through vertical advection, *Atmos. Chem. Phys.*, 23, 1705–1730, <https://doi.org/10.5194/acp-23-1705-2023>, 2023.
- Sassi, F., and Liu, H.-L. (2014). Westward traveling planetary wave events in the lower thermosphere during solar minimum conditions simulated by SD-WACCM-X. *Journal of Atmospheric and Solar - Terrestrial Physics*, 119, 11–26.
- Sassi, F., Siskind, D. E., Tate, J. L., Liu, H.-L., and Randall, C. E. (2018). Simulations of the boreal winter upper mesosphere and lower thermosphere with meteorological specifications in SD-WACCM-X. *Journal of Geophysical Research: Atmospheres*, 123, 3791–3811. <https://doi.org/10.1002/2017JD027782>
- Shapiro, A. V., Rozanov, E., Shapiro, A. I., Wang, S., Egorova, T., Schmutz, W., and Peter, Th (2012). Signature of the 27-day solar rotation cycle in mesospheric OH and H<sub>2</sub>O observed by the Aura Microwave Limb Sounder, *Atmos. Chem. Phys.*, 12, 3181–3188, <https://doi.org/10.5194/acp-12-3181-2012>, 2012.
- Teng, C. K. M., Gu, S. Y., Qin, Y. S., Dou, X. K., Li, N., and Tang, L. (2021). Unexpected Decrease in TW3 Amplitude During Antarctic Sudden Stratospheric



- 831 Warming Events as Revealed by SD-WACCM-X. Journal of Geophysical  
832 Research-Space Physics, 126(10), e2020JA029050.  
833 <https://doi.org/10.1029/2020JA029050>
- 834 Torre, de la, L., Garcia R. R., Barriopedro D., and A. Chandran (2012). Climatology  
835 and characteristics of stratospheric sudden warmings in the Whole Atmosphere  
836 Community Climate Model, J. Geophys. Res., 117, D04110,  
837 doi:10.1029/2011JD016840.
- 838 Tweedy, O. V., et al. (2013). Nighttime secondary ozone layer during major  
839 stratospheric sudden warmings in specified-dynamics WACCM, J. Geophys. Res.  
840 Atmos., 118, 8346–8358, doi:10.1002/jgrd.50651.
- 841 Wehrbein, W. M., & Leovy, C. B. (1982). An accurate radiative heating and cooling  
842 algorithm for use in a dynamical model of the middle atmosphere. Journal of  
843 Atmospheric Sciences, 39(7), 1532-1544.
- 844 Winick, J. R., Wintersteiner, P. P., Picard, R. H., Esplin, D., Mlynczak, M. G., Russell  
845 III, J. M., and Gordley L. L. (2009). OH layer characteristics during unusual boreal  
846 winters of 2004 and 2006, J. Geophys. Res., 114, A02303, doi:10.10
- 847 Xu, J., A. K. Smith, G. Jiang, H. Gao, Y. Wei, M. G. Mlynczak, and J. M. Russell III  
848 (2010). Strong longitudinal variations in the OH nightglow, Geophys. Res. Lett.,  
849 37, L21801, doi:10.1029/2010GL043972.
- 850 Yang, C., Smith, A. K., Li, T., and Dou, X. (2018). The effect of the Madden-Julian  
851 Oscillation on the mesospheric migrating diurnal tide: A study using SD-  
852 WACCM. Geophysical Research Letters, 45, 5105–5114.  
853 <https://doi.org/10.1029/2018GL077956>
- 854 Yang, J., Wang, J., Liu, D., Guo, W., and Zhang, Y.: Observation and simulation of  
855 neutral air density in the middle atmosphere during the 2021 sudden stratospheric  
856 warming event, Atmos. Chem. Phys., 24, 10113–10127,  
857 <https://doi.org/10.5194/acp-24-10113-2024>, 2024.
- 858 Yu, W., Garcia, R., Yue, J., Russell, J. III, and Mlynczak, M. (2022). Variability of water  
859 vapor in the tropical middle atmosphere observed from satellites and interpreted  
860 using SD-WACCM simulations. Journal of Geophysical Research: Atmospheres,  
861 127, e2022JD036714. <https://doi.org/10.1029/2022JD036714>



- 862 Yue, X., W. S. Schreiner, J. Lei, C. Rocken, D. C. Hunt, Y.-H. Kuo, and W. Wan (2010).  
863 Global ionospheric response observed by COSMIC satellites during the January  
864 2009 stratospheric sudden warming event, *J. Geophys. Res.*, 115, A00G09,  
865 doi:10.1029/2010JA015466.
- 866 Zhang, J., Limpasuvan, V., Orsolini, Y. J., Espy, P. J., and Hibbins, R. E. (2021).  
867 Climatological westward-propagating semidiurnal tides and their composite  
868 response to sudden stratospheric warmings in SuperDARN and SD-WACCM-X.  
869 *Journal of Geophysical Research: Atmospheres*, 126, e2020JD032895.  
870 <https://doi.org/10.1029/2020JD032895>
- 871 Zhang, J., Oberheide, J., Pedatella, N. M., and Liu, G. (2025). Impact of Arctic and  
872 Antarctic sudden stratospheric warmings on thermospheric composition. *Journal*  
873 *of Geophysical Research: Space Physics*, 130, e2024JA032562.  
874 <https://doi.org/10.1029/2024JA032562>  
875